



Core-shell nanostructured heteropoly acid-functionalized metal-organic frameworks: Bifunctional heterogeneous catalyst for efficient biodiesel production



Yukwon Jeon^{a,1}, Won Seok Chi^{a,1}, Jusoon Hwang^b, Do Hyun Kim^a, Jong Hak Kim^{a,*}, Yong-Gun Shul^{a,b,**}

^a Department of Chemical and Biomolecular Engineering, Yonsei University, Yonsei-ro 50, Seodaemun-gu, Seoul, 120-749, Republic of Korea

^b Department of Graduate Program in Climate Change Energy Engineering, Yonsei University, Yonsei-ro 50, Seodaemun-gu, Seoul, 120-749, Republic of Korea

ARTICLE INFO

Keywords:

Heterogeneous catalyst
Biodiesel production
Heteropoly acid
Zeolitic imidazolate framework
Core-shell structures

ABSTRACT

We developed a new class of acid-base bifunctional heterogeneous catalyst, which can be used in the transesterification of rapeseed oil for highly efficient biodiesel production. A simple Keggin-type HPA (heteropoly acid) functionalization on the surface of zeolitic imidazolate framework-8 (ZIF-8) nanoparticles, through an imidazolium medium, results in the bifunctional heterogeneous catalysts. The hybrid materials exhibit a novel hierarchically core-shell nanostructure, which provides a large surface area and interconnectivity, leading to a thin-wrinkled HPA shell at the surface of rhombic dodecahedral ZIF-8 core crystals. A strong O–N hybrid bonding through an electrostatic effect in the hybrid materials demonstrates a strong interaction between the Keggin and imidazole units, which is one of the main driving forces of hybrid materials formation. Additionally, the transformation of the HPA/ZIF-8 ratio in the hybrid materials changes the acidity and basicity, thereby affecting catalyst activity. We used these bifunctional core-shell materials as environmentally friendly heterogeneous catalysts in the transesterification of rapeseed oil with methanol to produce a high-quality biodiesel. Of particular interest, the HPA-functionalized ZIF-8 catalyst with a proper HPA/ZIF-8 ratio shows a high FAME conversion of 98.02% along with high recyclability because of the sufficiently large surface area and bi-functionality of strong acidity. Furthermore, the HPA-functionalized ZIF-8 catalyst shows a high reaction efficiency of the benzyl alcohol oxidation process, indicating a great potential of our catalyst to a wide range of applications.

1. Introduction

In recent years, bifunctional catalysts have been widely used for industrial fine chemical productions [1–3]. The concept of catalytic bifunctionality has been designed to drive complex reactions through the sophisticated strategy of combining two hostile functions, such as acid and base, with cooperative interactions between accurately positioned functional groups in their active sites [4–8]. Nowadays, artificial materials as heterogeneous catalysts have been developed to address a stimulation of a real challenge and perform multistep or consecutive reactions by immobilized mutually incompatible two-disparate active sites. These increase the overall reaction rate that would not be achievable using either of the catalytic species independently. The

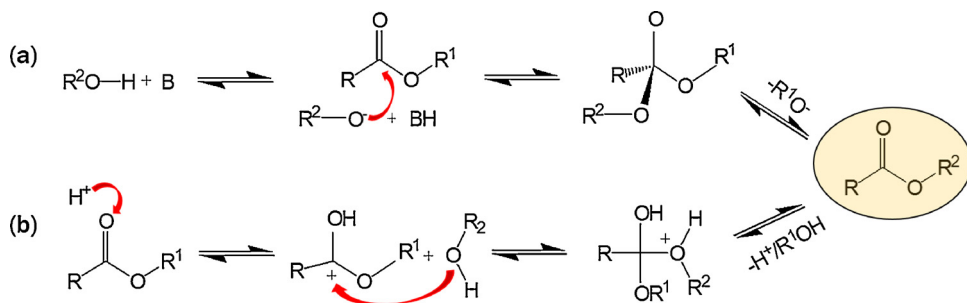
bifunctional catalytic property can be especially efficient for the process of transesterification for biodiesel production [9–11]. Transesterification is the process of changing the organic group of R^o at an ester to the organic group of R' at an alcohol (generally methanol) to produce fatty acid methyl ester (FAME) and an impure co-product, glycerol [12–15]. There are two different reaction pathways catalyzed by the addition of base or acid catalysts, as from the basic routes shown in Scheme 1. (a) The base catalysts catalyze the reaction by deprotonating the alcohol from the activation of the nucleophilicity, whereas (b) the strong acid catalysts protonate the carbonyl group to make it a more potent electrophile. However, reports on the design of a bifunctional catalyst and the mechanism of the unique combined reaction pathway, which may increase the efficiency of biodiesel production by the acid-base synergy

* Corresponding author.

** Corresponding author at: Department of Chemical and Biomolecular Engineering, Yonsei University, Yonsei-ro 50, Seodaemun-gu, Seoul, 120-749, Republic of Korea/Department of Graduate Program in Climate Change Energy Engineering, Yonsei University, Yonsei-ro 50, Seodaemun-gu, Seoul, 120-749, Republic of Korea.

E-mail addresses: jonghak@yonsei.ac.kr (J.H. Kim), shulg@yonsei.ac.kr (Y.-G. Shul).

¹ These authors contributed equally to this work.



Scheme 1. Reaction pathway of the transesterification with rapeseed oil under the (a) base and (b) acid environments.

and cooperative effects, are limited.

To date, heteropoly acids (HPAs) have been recognized as economically and environmentally benign acid catalysts due to their acidity and redox properties for various reactions [16–18]. However, the use of HPAs is limited because of its low surface area, high solubility, low thermal stability, and difficulties in fabrication of chemically antagonistic functions, which are crucial points to utilize HPA as a counter-acid for the design of the acid–base heterogeneous bifunctional catalysts. To overcome these problems, the ion-exchanged HPA, with tunable antagonistic functions and modifications to a large surface area support, have been studied by utilizing various supports such as mesoporous silica, carbon, and zeolite [7–11,19–22]. For example, a mesoporous silica can be modified with a site-isolated functional group to stabilize the HPA. In addition, a designation of acid–base HPA catalysts can be synthesized by incorporating rare-earth-metals into the heteropoly structure, which has tunable antagonistic functions for highly efficient one-pot tandem reactions. However, it is still difficult to control the spatial arrangement of the incompatible functional groups with a high concentration. Furthermore, better stability is essential for the catalyst reusability especially at a solid catalyst system.

Herein, we designed a novel hierarchically core-shell structure by a chemical HPA coverage on the imidazolium based ZIF-8. A different approach from previous works by using MOF was developed to form bifunctional catalysts for the transesterification to produce a highly concentrated biodiesel [23–25]. Using a simple HPA-functionalization method, we were able to maintain the benefits of ZIF-8 nanoparticles such as the large surface area, chemical and thermal stability, and tunable functions (i.e., acid and base). A strong chemical bond between the HPA and ZIF-8 leads to stable hybrid materials, which possess both a large surface area and good stability at high temperature and toward various solvents. Thus, we were able to achieve a bi-functionality from the acidity of the HPA (and a part of the Zn in ZIF-8) and basicity of the imidazolate, which was highly related to the total FAME production and product distribution by dual mechanism. The optimized HPA-functionalized ZIF-8 core-shell bifunctional catalyst showed a great performance in biodiesel production with reliable recyclability as well as a high catalytic activity on benzyl alcohol oxidation, which demonstrates the possibilities to broader application area.

2. Experimental section

2.1. Synthesis of ZIF-8

Zn(NO₃)₂·6H₂O (3 g) and 2-methylimidazole (6.9 g) were dissolved in separate methanol solvents (100 mL). The separate solutions were mixed rapidly and were vigorously stirred at room temperature for 1 h. The synthesized ZIF-8 nanoparticles were centrifuged (12,000 rpm, 30 min) and washed with fresh methanol. We repeated this procedure at least three times for a thorough washing process to completely remove residues and remaining solvents. The white ZIF-8 nanoparticles were dried in an oven at 50 °C overnight then activated in a vacuum oven at 180 °C for 16 h.

2.2. Synthesis of HPA-functionalized ZIF-8 nanoparticles bifunctional catalysts

Different amounts of heteropoly acid (0, 0.05, 0.1, 0.3, 0.5 g) were dissolved in DI-water (10 ml), respectively. The previously prepared ZIF-8 nanoparticles (each 0.1 g) were added to the HPA solutions, and we followed a sonication process for 30 min to enable well-distribution. These heterogeneous solutions were stirred for 24 h at room temperature. Products were centrifuged (12,000 rpm, 30 min) and washed a few times with DI-water. The final products were dried in a vacuum oven at 100 °C to eliminate DI-water solvents. We refer to the HPA-functionalized ZIF-8 nanoparticles as HZN corresponding to HPA amounts in synthesis. The HZN-'number' indicates the HPA-functionalized ZIF-8 nanoparticles prepared with specific heteropoly acid amounts (HZN-1 is from 0.05 g HPA addition, HZN-2 is from 0.1 g HPA addition, HZN-3 is from 0.3 g HPA addition, and HZN-4 is from 0.5 g HPA addition).

2.3. Material characterizations

Field-emission scanning electron microscopy (FE-SEM) images were obtained with a SUPRA 55 VP (Carl Zeiss) after the platinum sputtering at 10 mA for 100 s of samples for thin conducting layer deposition. Energy-filtering transmission electron microscopy (EF-TEM) images were examined using a LIBRA 120 microscope (Carl Zeiss) operating at 120 kV. For TEM sample preparation, solid powders were dispersed in methanol solvent with 0.5% concentration by ultra-sonication. A drop of the solution was cast onto a TEM copper grid and dried in an oven at 50 °C to evaporate the solvent. High-resolution transmission electron microscopy (HR-TEM) images equipped with energy dispersive spectroscopy (EDS) element mapping and line-patterning capability were used to confirm the core-shell structure. The nitrogen adsorption/desorption isotherms at 77 K, to determine the surface area and total pore volume, were collected using a BELSORP-mini (BEL Japan Inc.) XRD measurement, performed with a D8 advance (Bruker) operated with a Cu Kα radiation source ($\lambda = 1.541 \text{ \AA}$) at 40 kV and 300 mA. TGA measurement was carried out with a TA instrument from 50 to 800 °C at a scan rate of 20 °C/min under air atmosphere. Fourier transform infrared (FT-IR) spectra were collected with Spectrum 100 (PerkinElmer) using an attenuated total reflectance (ATR) accessory. X-ray photoelectron spectroscopy (XPS) was measured using a K-alpha XPS spectrometer (Thermo) with a monochromatic Al Kα X-ray source. The binding energies of C 1 s, N 1 s, O 1 s, P2p, W4f and Zn2p were calibrated based on the graphitic C 1 s peak at 285 eV. The XPS peaks were fitted by the Fityk program using Shirley background subtraction and Gaussian function. Moreover, the X-ray absorption spectroscopy (XAS) was also performed for each element of Zn L_{III}-edge, C K-edge, N K-edge, and O K-edge spectra at beamline 10D (Bending magnet, Phoibos 150), Pohang Accelerator Laboratory (PAL). Measurements were made with solid samples at room temperature.

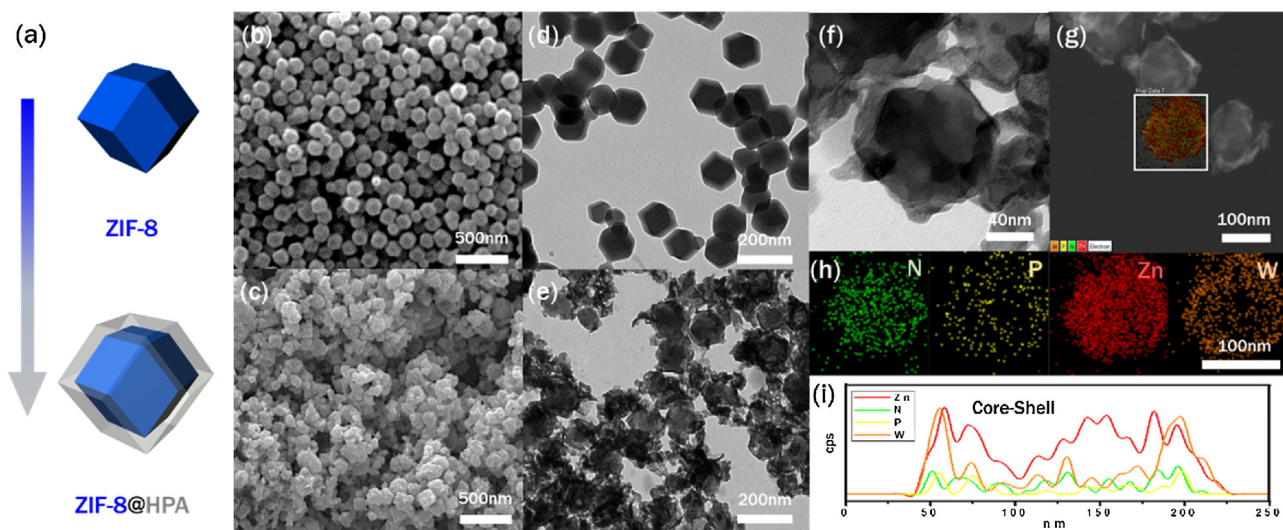


Fig. 1. (a) Schematic illustration for HPA-functionalization onto ZIF-8 nanoparticles, SEM images for (b) pure ZIF-8, (c) HZN-2, TEM images for (d) pure ZIF-8, (e) HZN-2, (f) HR-TEM images for HZN-2, (g) HR-TEM images with EDS element mapping for HZN-2, (h) EDS mapping according to N, P, Zn, and W elements for HZN-2, and (i) EDS line-patterning according to N, P, Zn, and W elements for HZN-2.

2.4. Procedure for NH_3 and CO_2 TPD

The NH_3 and CO_2 adsorptions using Bel-Cat-M (BEL JAPAN, INC.) were applied to measure the acidic and basic properties, respectively. Both measurements were conducted under the same conditions. In each case, 50 mg of sample was loaded and first treated at 100 °C for 60 min under He condition (50 ml). Then, it was flushed with NH_3 or CO_2 at 80 °C for 60 min and cooled to room temperature. The measurements of the NH_3 and CO_2 adsorptions to investigate the acidic and basic properties were performed under He gas with the temperature range of 25 °C to 850 °C at 5 °C/min and held at this value for 10 min. Each effluent gas was continuously analyzed for NH_3 and CO_2 using a thermal conductivity detector.

2.5. Procedure of biodiesel production

Catalytic activity of the prepared bifunctional catalysts was performed by rapeseed oil transesterification. 10 g of rapeseed oil and 0.4 g of catalyst (4 wt.%) were loaded into a batch reactor (HR-8200, Hanwoul) and vigorously stirred. After the mixture was mixed evenly, a certain amount of methanol (1:10 = oil:methanol) was added. The heat-controlled batch reactor was started to heat up to the testing reaction temperature under a continuous stirring. Then, it was held for 2 h at each temperature with a range of 80 to 240 °C. After the transesterification reaction finished, the products were separated with the heterogeneous catalyst by a filtration process, and then the esters in the products were extracted by the addition of dichloromethane solvent in organic phase. The dichloromethane was removed from the organic layer by heating at 70 °C. The filtered catalysts were washed and dried to perform the regeneration tests (5 times) and post-characterization.

The content in FAME of the organic layer was determined by following the European regulated procedure EN 14103. Basically, 250 mg of the organic layer was added to 5 mL of heptane (C7) solution of the internal standard methyl heptadecanoate (10 g/L of C17 ester in heptane). This solution was analyzed in an ACME 6000 GC equipped with a GL Science InertCap® WAX capillary column using helium as a carrier gas. F.A.M.E. Mix, C8-C24 (Sigma-Aldrich) was used as an analytical standard. The FAME content (wt.%) was calculated from the formula:

$$\text{FAME Contents(wt\%)} = \frac{(\sum A_i - A_{Mh})}{A_{Mh}} \times \frac{C_{Mh} \times V_{Mh}}{m} \times 100$$

where $\sum A_i$ is the total peak area from methyl esters, from methyl

octanoate (C8:0) to methyl lignocerate (C24:0); A_{Mh} the area of methyl heptadecanoate, of which the response factor is equal to those of FAME; C_{Mh} the concentration in mg/mL of the methyl heptadecanoate (10 mg/ml); V_{Mh} the volume in mL of the methyl heptadecanoate solution (5 ml); m is the weight in mg of the sample. All the main transesterification products of the methyl esters were methyl octanoate (C8:0), methyl decanoate (C10:0), methyl laurate (C12:0), methyl myristate (C14:0), methyl palmitate (C16:0), methyl palmitoleate (C16:1), methyl stearate (C18:0), methyl oleate (C18:1), methyl linoleate (C18:2), methyl linolenate (C18:3), methyl arachidate (C20:0), methyl behenate (C22:0), methyl erucate (C22:1), and methyl lignocerate (C24:0).

2.6. Procedure of benzyl alcohol oxidation

The catalytic oxidation of benzyl alcohol was carried out in a 50 ml round-bottom flask fitted with a water-circulated condenser. For the typical reaction, 4.6 mmol of benzyl alcohol and 6.0 mmol 30% H_2O_2 were mixed at a stirring condition. The mixture was heated in an oil bath to the fixed temperature of 75 °C. Then, 4.6 mmol of the catalyst was added to the hot mixture and kept for 2 h. After the reaction finished, the heterogeneous catalyst was removed from the mixture by filtration. The final product was separated and diluted with a certain amount of ethanol. The mixture was analyzed by GC (ACME 6000 GC) equipped with a flame ion detector and HP-INNOWAX capillary column (film thickness: 0.5 mm; i.d.: 0.32 mm; length: 30 m) using helium as a carrier gas. The conversion was calculated as the number of moles of reacted benzyl alcohol per mole of non-reacted benzyl alcohol, and, the selectivity was calculated as the number of moles of produced benzaldehyde per mole of reacted benzyl alcohol.

3. Results and discussion

3.1. Core-shell morphology

We synthesized ZIF-8 nanoparticles using a zinc precursor and 2-methylimidazole via a solvothermal reaction under ambient conditions following a previously reported method [26]. Although the ZIF-8 nanoparticles have a large surface area and good chemical/thermal stability, they are impossible for the direct use as a catalyst due to a lack of catalytic functionality. To address this issue, we simply functionalized ZIF-8 nanoparticles with heteropoly acid (HPA) through an imidazole-medium chemical interaction to create catalytic hybrid materials, as

Table 1

Elementary data from the XPS and textural properties from the N₂ adsorption isomers characterizations for pure ZIF-8, pure HPA, and HZN-1, 2, 3, and 4.

	Element Compositions ^a						N ₂ adsorption isomers		
	C	N	Zn	O	P	W	S _a ^b	V _T ^c	P _a ^d
ZIF-8	50.7	22.9	19.3	7.1	—	—	1712.8	1.51	3.5
HZN-1	42.6	14.9	15.8	25.4	0.3	2.8	805.6	0.61	3.0
HZN-2	40.9	13.5	13.3	28.3	0.6	3.8	457.1	0.38	3.3
HZN-3	38.9	12.8	12.7	30.0	0.8	4.8	74.2	0.13	7.1
HZN-4	33.2	11.1	11.6	35.9	1.1	7.2	17.5	0.12	27.7
HPA	24.8	—	—	52.7	2.2	19.6	0.5	0.003	21.7

^a Element compositions from the XPS measurements.

^b BET surface area (m²/g).

^c Total pore volume (p/p₀ = 0.927).

^d Average pore diameter (nm).

shown in Fig. 1(a). In the synthetic process, we also controlled HPA concentration to prepare various ratios of HPA to ZIF-8 nanoparticles in hybrid materials to find out the best HPA concentration for efficient catalyst production. We refer to the HPA-functionalized ZIF-8 nanoparticles as HZN-'number' according to HPA concentrations with increasing trend. For instance, HZN-1, 2, 3, and 4 mean HPA-functionalized ZIF-8 nanoparticles with the corresponding HPA concentrations of 0.05, 0.1, 0.3, and 0.5 g, respectively. We calculated the ratio of ZIF-8 over HPA based on the relative XPS peak intensities between ZIF-8 (C 1s, N 1s) and HPA (P 2p, W 4f, O 1s), shown in Table 1. The actual HPA concentration trend in HZN-1, 2, 3, and 4 matches well with our original experimental design. Of note, HZN are insoluble in polar solvents (i.e., water or methanol), which dissolve HPA well, therefore we could employ the HZN in common solvents for catalyst application. Fig. 1(b) shows 100–200 nm sized ZIF-8 nanoparticles with narrow particle size distribution. Fig. 1(c) shows HZN with a rough surface configuration induced by HPA introduction, but which still retain a similar particle size than that of the pure ZIF-8 nanoparticles. As HPA concentration increases in a synthetic procedure, the HZN present a broad particle size distribution due to the agglomeration between mutual particles, as shown in Fig. S1. We took a SEM image of pure HPA as a reference, as well as images of pure ZIF-8 nanoparticles and HZN. The pure HPA coated on the glass substrate via a solvent evaporation shows dense layers with large cracks that originated during solvent evaporation, as in Fig. S1(f). This indicates that ZIF-8 nanoparticles offer a large surface area so the catalyst can enhance possible active sites where the catalytic reaction happens. Fig. 1(d, e) presents TEM images for pure ZIF-8 nanoparticles and HZN, respectively. Comparing all the TEM images in Fig. S2, the pure ZIF-8 nanoparticles show rhombic dodecahedron morphology with a smooth surface, whereas the HZN show two separate portions including a dark region inside due to the high electron density of ZIF-8 nanoparticles and a bright region outside due to the low electron density of HPA, resulting in a core-shell structure. The core (dark region) has a diameter of 100–200 nm, which is well-matched with that of ZIF-8 nanoparticles, and the shell (bright region) has thin-wrinkled structure providing a large surface area and interconnectivity. Fig. 1(f) shows the HR-TEM image for HZN that indicates a core-shell structure from the dark region according to ZIF-8 nanoparticle positions at the center of the particles. For accurate information, we further demonstrate the core-shell structure of HZN with EDX mapping and line patterning from the HR-TEM images, shown in Fig. 1(g–i). The Zn and N elements from the ZIF-8 nanoparticles are located at the core side, while the W and P elements from the HPA are placed at the shell side, indicating a core (ZIF-8 nanoparticles)-shell (HPA) structure. Moreover, the line-patterning shows strong W and P element peak intensities at 50 nm and 200 nm over the range of the line, indicating the HPA covers the surface of 100–150 nm sized ZIF-8 nanoparticles. Of note, the low peak intensities of the Zn element, from 50 nm to 200 nm, indicate a partial decomposition of the ZIF-8 nanoparticles. The formation of the

core-shell architecture of HZN-1, 2, 3, and 4 was demonstrated by the EDX mapping and line-patterning, as shown in Figs. S3–S7.

3.2. Physical property

Fig. S8(a) presents TGA curves for pure ZIF-8, pure HPA, and HZN-1, 2, 3, and 4 with a heat flow up to 700 °C. The ZIF-8 nanoparticles retained their weight up to 400 °C with a small weight loss due to remained solvent evaporation (i.e., water and methanol). Following this sudden weight loss, around 400–450 °C, the ZIF-8 nanoparticles convert into ZnO particles through an oxidation process [26]. The removal of organic components in the ZIF-8 nanoparticles, and the oxidation of Zn ions via a high-temperature annealing process, leads to a final weight of pure ZIF-8 nanoparticles to 40 wt%. Pure HPA exhibits two main drops in weight resulting from weakly bound water from 25 °C to 100 °C as the first step, and strongly bound water from 100 °C to 200 °C as the second step, owing to a large water crystallization attachment [27,28]. After the water detachment, pure HPAs maintain their weight at a high-temperature range (> 200 °C) attributable to its crystal structure based on heat resistant characteristics [29]. The high thermal stability of pure HPA affects the HPA-functionalization which contributes to an increase in the thermal stability of pure ZIF-8 nanoparticles at high temperatures. Fig. S8(b) shows the nitrogen adsorption-desorption isotherm for pure ZIF-8 nanoparticles, pure HPA, and HZN-1, 2, 3, and 4. We also include specific parameters related to nitrogen sorption isotherm such as BET surface area, total pore volume, and mean pore diameter, shown in Table 1. The nitrogen sorption isotherms for pure ZIF-8 nanoparticles, and HZN-1 and 2 show a sudden increase in nitrogen adsorption in the low P/P₀ range (< 0.05), indicating the presence of a microporous structure [30,31]. Contrarily, the sudden increase disappears in the nitrogen sorption isotherm for HZN-3 and 4, and pure HPA resulting from a collapsed microporous structure and blocked pores in the ZIF-8 nanoparticles due to excessive HPA addition. Nevertheless, HZN-3 and 4 show a hysteresis loop at P/P₀ = 0.9–1 because of capillary condensation. This indicates that the HZN with high HPA concentration still possess a mesoporous structure, even though the microporous structure decomposes. In terms of the BET surface area, pure ZIF-8 nanoparticles show 1712 m²/g and HZN show a decreased surface area relative to that of the pure ZIF-8 nanoparticles (HZN-1, 2, 3, and 4 show 805, 457, 74, and 17 m²/g, respectively). In addition, the HZN exhibit a reduced total pore volume with a HPA content increase.

3.3. Crystal and chemical binding structure

Fig. 2(a) shows the FT-IR spectra for pure ZIF-8, pure HPA, and HZN-1, 2, 3, and 4. The pure ZIF-8 nanoparticles exhibit sharp absorption bands at 1146 cm⁻¹ and 421 cm⁻¹, corresponding to C–N stretching vibration and Zn–N stretching vibration modes, respectively, indicating successful ZIF-8 formation. The pure HPA presents four Keggin structure characteristic absorption bands at 1075 cm⁻¹ for P–Oa, 974 cm⁻¹ for W=Od, 887 cm⁻¹ for W–Ob–W, and 735 cm⁻¹ for W–Oc–W [32–34]. The HZN show shifted Keggin structure peaks to higher wavenumbers due to chemical interaction with the ZIF-8 nanoparticles compared to those of pure HPA. For example, HZN-1, which has the smallest HPA content, exhibits the Keggin structure peaks at 1080 cm⁻¹ for P–Oa, 994 cm⁻¹ for W=Od, 884 cm⁻¹ for W–Ob–W, and 808 cm⁻¹ for W–Oc–W, respectively. These results reveal that various HPA concentrations in a synthetic method for HZN production induce varied degrees of chemical interaction between HPA and ZIF-8 nanoparticles. Of note, the Zn–N stretching vibration at 421 cm⁻¹ disappears in the FT-IR for HZN-4, which indicates the frameworks, consisting of metal ions and organic ligands, completely decompose. This result also matches the low BET surface area of HZN-4 sample (~17 m²/g), showing a barely porous structure. Fig. 2(b) presents the XRD patterns for the pure ZIF-8 nanoparticles, pure HPA, and HZN-1, 2,

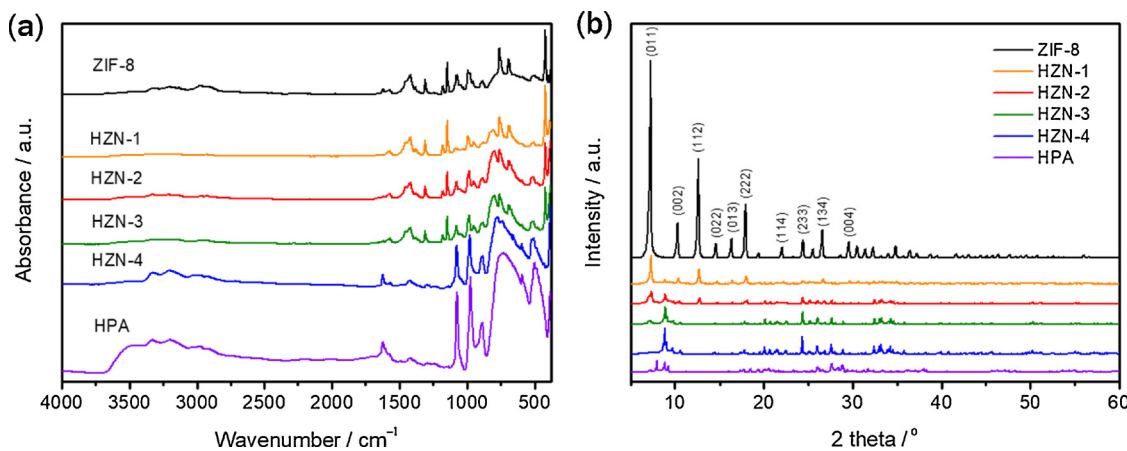


Fig. 2. (a) FT-IR spectra, and (b) XRD pattern for pure ZIF-8, pure HPA, and HZN-1, 2, 3, and 4.

3, and 4. The pure ZIF-8 nanoparticles exhibit crystalline phase characteristics with assignments such as (011), (112), and (222), which show strong peak intensities. Overall, as the HPA content increases, the HZN shows a decrease in the peak intensities of the ZIF-8 characteristic phase and formation of the HPA crystalline peak in the XRD patterns. The HZN with moderate HPA addition (i.e., HZN-1 and 2) maintain the characteristic peaks of pure ZIF-8 nanoparticles. The main characteristic peak of the ZIF-8 nanoparticle disappears in the XRD pattern of HZN-3 except a small crystalline peak around 7.1° for the (011) phase. This result matches with the trend of nitrogen adsorption/desorption isotherm, which demonstrates an absence of micropores. When the HPA content is further increased from HZN-3 to HZN-4, the remaining small crystalline peak for the (011) phase completely disappears, corresponding to the disappearance of the Zn–N bond in the FT-IR spectra. In terms of characteristic HPA peaks, the XRD pattern for pure HPA is assigned to the HPA with 14 hydrated Keggin anions after drying. Interestingly, however, this original structure transforms to the 6 hydrated Keggin anions for all HZNS, with a relatively large peak at 8.9° [35]. This change in the water network generally happened by the surface charges and hence by the substitution and nature of counter ions, which give a clue to a new bond with the surface of the ZIF-8 nanoparticles [35,36].

We also investigate the chemical bonding structure of HZN-1, 2, 3, and 4 using X-ray photoelectron spectroscopy (XPS) and X-ray absorption near edge structure (XANES) measurements. Fig. S9 shows that the XPS peak intensities for ZIF-8 (C 1s, N 1s) and HPA (P 2p, W 4f, O 1s) change as the ZIF-8 and HPA amounts change with the desired ratios. Moreover, the normalized XPS peaks in comparison with the XANES spectra (C K-edge, N K-edge, Zn L-edge, and O K-edge) demonstrate changes in chemical bonding. The XPS peaks for pure HPA, pure ZIF-8 nanoparticles, and HZN-1, 2, 3, and 4 are also fitted to certain chemical bonding, as shown in Fig. 3(a-d), and the calculated compositions are summarized in Table S1. Pure HPA mainly contains the O²⁻ (W–O) and W⁶⁺ characteristic chemical states, which are assigned from the peaks at 530.59 eV, 36.33 eV, and 38.48 eV, respectively [37]. After HPA functionalization on the ZIF-8 nanoparticles, the binding energies of W 4f and O 1s in the HPA both shift to higher values (Fig. 3(a, b)), indicating a change in chemical bonding. Since the HPA is entirely protonated in water, as in our synthesis conditions, we can assume that the shifts of binding energies are formed by the interaction between the ZIF-8 surface and protonated HPA in water. From the shift in binding energies of the ZIF-8, we are able to demonstrate which site may interact and produce a strong bonding with the protonated HPA, especially O at the outer side. As for the XPS spectra related to the ZIF-8 structure, the binding energy of Zn 2p in Fig. S10(a) does not exhibit a significant shift, indicating weak interaction with the HPA. The N 1s and C 1s in Fig. 3(c-d) show significant and slight shifts, respectively,

suggesting that the N species are highly protonated from a strong O (from the HPA surface)-N hybrid bonding through an electrostatic effect. The convoluted peaks exhibit formation of the N–C–O and N–O bonds (N 1s) at around 400.1 and 401.2 eV, respectively [38,39], supported by the increase of the C–N–O bond strength for C 1s at around 287.1 eV [40]. Additionally, these changes are related to a significant shift of the O 1s peak, leading to the production of the W–O–N and N–O–N bonds at around 531.5 and 532.4 eV, respectively, thereby producing a basicity for the transesterification reaction. To further confirm the chemical structure of the HZN, we investigated the XANES peaks of the C K-edge, N K-edge, Zn L-edge, and O K-edge for pure HPA, pure ZIF-8, and HZN-1, 2, 3, and 4. In Fig. S10(b), we were not able to detect any noticeable change in the Zn L-edge, while the HZN indicated an absence of interaction through the Zn species. As shown in Fig. 3(e), the bonding feature of the C=N–C bond at around 286.4 eV in the C K-edge gradually disappeared as more HPA interacted with ZIF-8, which may indicate a change in the N species bonding structure during the formation of the core-shell structure [41]. The most noticeable evidence was observed in Fig. 3(f), in which the N K-edge shows a new characteristic peak formation, assigned as the Zn(C=O)N bond at around 400.7 eV, after HPA functionalization onto ZIF-8 nanoparticles, following a gradual disappearance of the main C=N–C bond at around 399.6 eV. Additionally, Fig. 3(g) presents that the O K-edge shows a new characteristic peak related to the formation of the W–O–N bond at 539.1 eV, while the main HPA peak of W–O at 532.4 eV relatively decreased [42,43]. Overall, the XPS and XANES results demonstrate that changes of the chemical bonding structure provide a strong clue that the outer O element in the HPA ionically reacts with the non-bonded N in the ZIF-8, as illustrated in Fig. 4. Based on a new bonding formation, the HZN obtain new property sets such as high thermal stability and insolubility in popular hydrophilic solvents, which are crucial characteristics in heterogeneous catalysis.

The HZN possess a stable bi-functionality with acid and basic sites, which may provide a two-way biodiesel production from the transesterification of rapeseed oil, thereby increasing production efficiency. Fig. 5 presents exposed catalytic sites from the acidity (a) and basicity (b) capacities for pure HPA, pure ZIF-8 and HZN-1, 2, 3, and 4 using the NH₃ and CO₂ temperature programmed desorption (TPD) techniques. The total acidity and basicity capacities are defined by the intensities and integration of the peaks in Table 2, which can be calculated by the peak integration from the divided temperature range before and after 200 °C [44–46]. The HZN show a bi-functionality resulting from the acidity of HPA (and a part of the Zn in ZIF-8) and basicity of the imidazolate in ZIF-8. Of note, the total basicity of 22.82 mmol/g from the pure ZIF-8 is approximately half compared to the total acidity of 41.95 mmol/g from the pure HPA, along with a small acidity from pure ZIF-8 (4.26 mmol/g). Thus, the high HPA content in HZN increases the

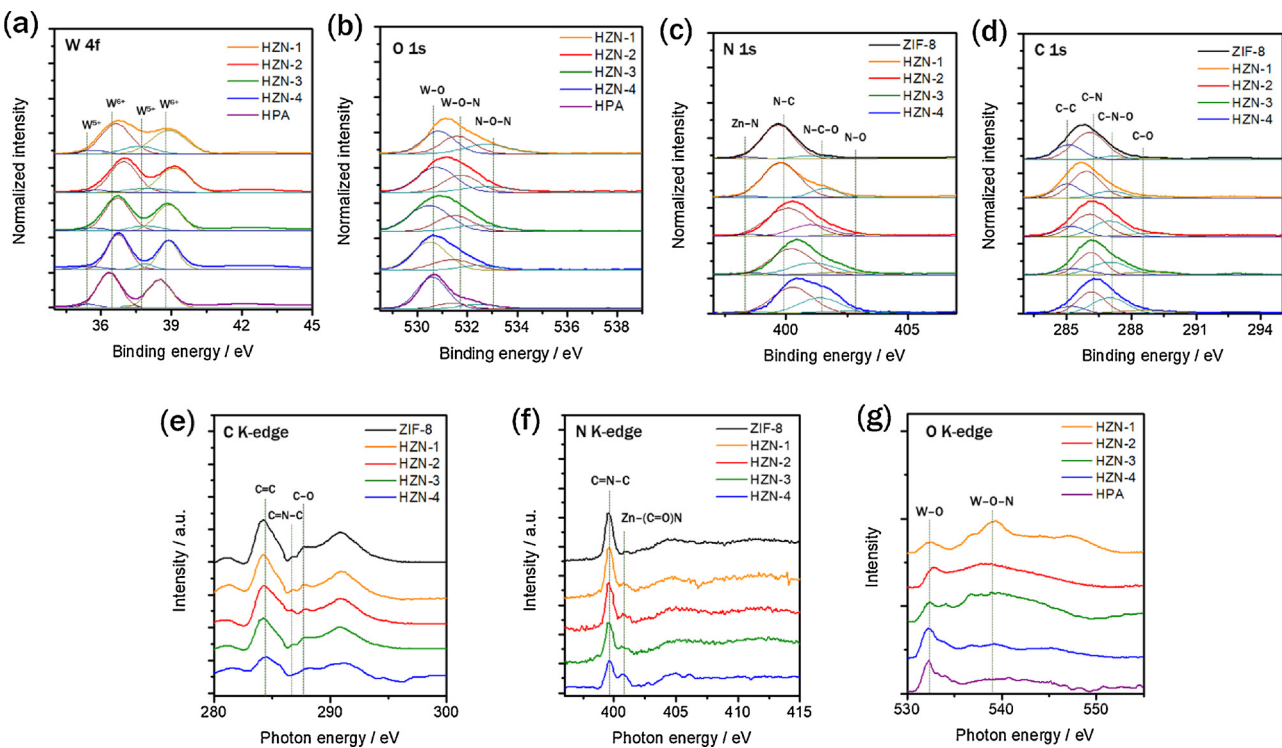


Fig. 3. Normalized and fitted XPS spectra of (a) W 4f, (b) O 1s, (c) N 1s, (d) C 1s, and XANES spectra of (e) C K-edge, (f) N K-edge, (g) O K-edge for pure ZIF-8, pure HPA, and HZN-1, 2, 3, and 4.

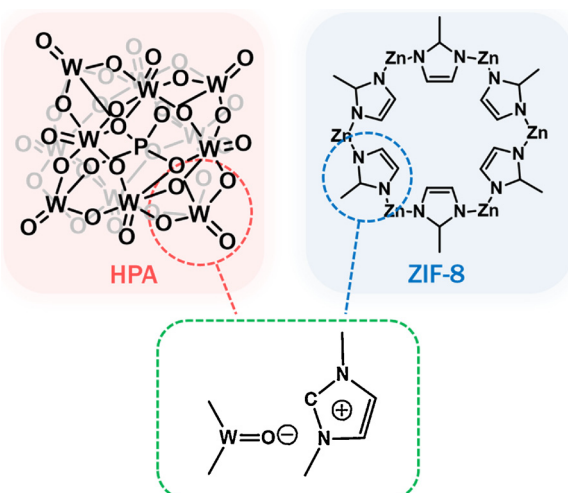


Fig. 4. Illustration of the plausible chemical bonding structure for the hybrid ZIF-8/HPA bifunctional catalyst for the transesterification of rapeseed oil.

total acidity capacities and vice versa. We separate the TPD peaks into relatively weak and strong acidity/basicity values. Of particular interest, the ratio of weak/strong basicity is close to around 3:7 regardless of the HPA composition in the HZN, shown in Table 2. The strong acidity increases from pure ZIF-8 nanoparticles to HZN-2 with a ratio change from around 8:2 to 6:4, resulting from a change in the bonding structure where the nitrogen and oxygen bonding influence the acidity and basicity. It was clearly seen that the richness of weak acidity (as from HPA) and medium strong basicity (as from ZIF-8) do not have an influence on the improved activity. On the other hand, the balanced acidity in both density and strength as well as strong basicity accounts for the best performance on HZN-2. Therefore, we could understand that these unique chemical property sets assist in demonstrating a new reaction mechanism using an acid-base synergy effect for efficient

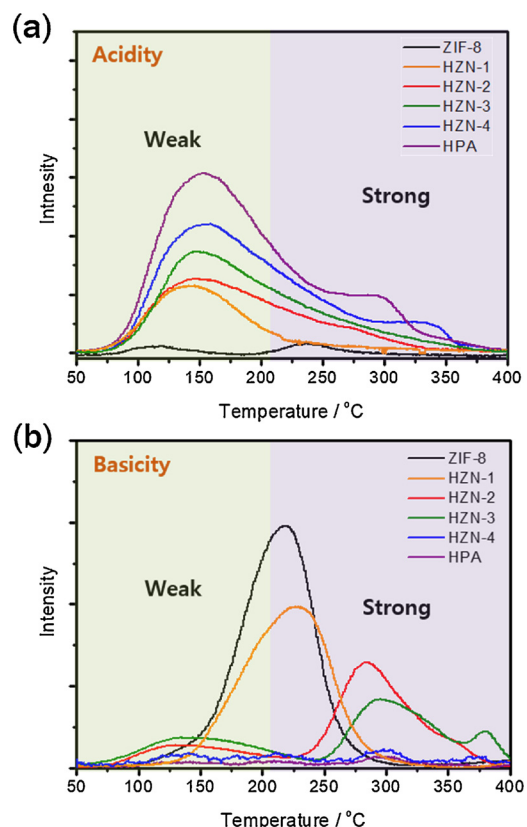


Fig. 5. (a) NH₃-TPD and (b) CO₂-TPD for pure ZIF-8, pure HPA, and HZN-1, 2, 3, and 4.

Table 2

Capacities and Compositions of the Acidity and Basicity calculated from the NH₃-TPD and CO₂-TPD, respectively, for pure ZIF-8, pure HPA, and HZN-1, 2, 3, and 4.

Catalysts	Acidity Capacity and Composition			Basicity Capacity and Composition		
	Total (mmol/g)	Weak (%)	Strong (%)	Total (mmol/g)	Weak (%)	Strong (%)
ZIF-8	4.26	82.41	17.64	22.82	35.22	64.81
HZN-1	11.85	81.1	18.93	18.24	32.21	67.82
HZN-2	17.44	64.62	35.41	15.03	31.94	68.14
HZN-3	22.60	62.12	37.95	12.39	30.12	69.92
HZN-4	30.85	62.74	37.32	3.85	32.33	67.71
HPA	41.95	63.55	36.51	0.68	30.62	69.4

biodiesel production.

3.4. Evaluation of biodiesel production

We tested the transesterification of rapeseed oil with a short-chain alcohol (i.e., methanol) at an oil:methanol molar ratio of 10:1 together with a 4 wt% catalyst. The most important factor relevant to catalytic activity is the total amount of FAME content (%), which is how much rapeseed oil converts to a biodiesel. Fig. S11 shows the total FAME contents for pure HPA, ZIF-8, HZN-2, and commercial MgO at temperatures from 80 to 240 °C in increments of 40 °C for a reaction time of 2 h. Overall, when the working temperature increases to 200 °C, all catalysts show improved catalytic properties due to enhanced activation energy and mass transfer resistance. The HZN showed a significant increase in the FAME conversion of over 95% due to simultaneous acid and basic functionalities with a large surface area, whereas the pure HPA and ZIF-8 catalysts showed low catalytic activation, especially the pure ZIF-8 which was not active even after 120 °C. Fig. 6(a–b), summarized from Table S2, present the total FAME contents and main compositions from the transesterification of rapeseed oil at an optimum

working temperature of 200 °C with a 2 h reaction time for pure HPA, ZIF-8, and HZN-1, 2, 3, and 4. In Fig. 6(a), as both acid and basic sites become active, the pure HPA and ZIF-8 show the FAME contents of 63.4% and 32.9%, respectively, from the transesterification reaction. A limitation of the homogeneous HPA is its difficulty to activate the main reaction of the long-chain esters transesterification due to the steric and conformational effects [47]. Meanwhile, despite ZIF-8 having a large surface area, it does not exhibit high catalytic properties because of its low acidity and basicity, as shown in Table 2. The HZN-2 with a large surface area of 457.02 m²/g, and both acidic and basic sites achieve the highest FAME conversion of 98.02%, probably also affected by a strong acidity formation in the bifunctional catalyst structure. This FAME conversion efficiency is even higher than that of the commercial MgO catalyst that has been known as a famous active reference for the transesterification of rapeseed oil [48,49]. Also, the obtained value is higher or comparable with those of state-of-the-art catalysts, as summarized in Table S3. After the HPA concentration was increased further, the HZN show similar catalytic activity to the homogeneous HPA due to a reduced surface area resulting from a collapsed porous structure. These results indicate that the acidic and basic bi-functionality

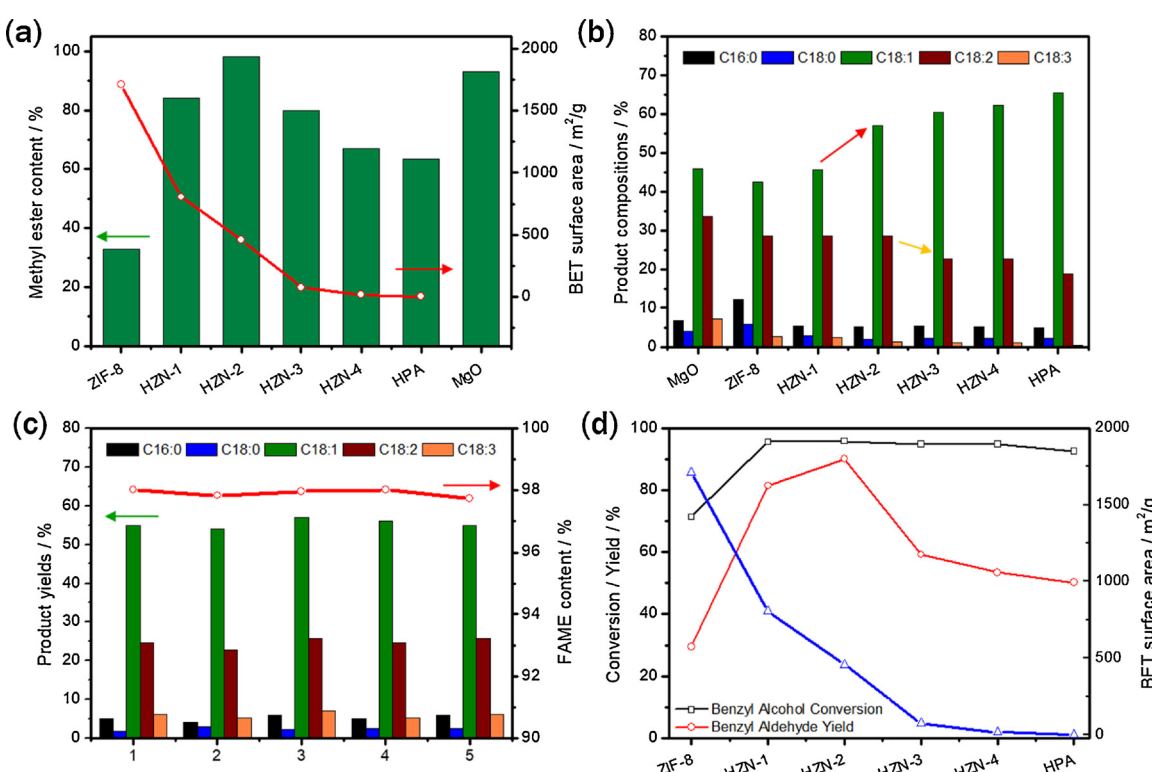


Fig. 6. (a) FAME contents from the transesterification of rapeseed oil and BET surface areas and (b) selected product compositions (C16:0, C18:0, C18:1, C18:2, C18:3) for MgO commercial, pure ZIF-8, pure HPA, and HZN-1, 2, 3, and 4. (c) Recyclability of the transesterification of rapeseed oil by the HZN-2 for 5 cycles with selected product yields and FAME contents. (d) Benzyl alcohol oxidation results of the benzyl alcohol conversion and benzyl aldehyde yield and BET surface areas for pure ZIF-8, pure HPA, and HZN-1, 2, 3, and 4.

and sufficient surface area of the HZN have synergistic effects on a great enhancement of FAME conversion efficiency in the transesterification process. In Fig. 6(b), we further investigate changes in the composition of the main products, such as methyl palmitate (C16:0, CH₃(CH₂)₁₄COOH), methyl stearate (C18:0, CH₃(CH₂)₁₆COOH), methyl oleate (C18:1, CH₃(CH₂)₇CH = CH(CH₂)₇COOH), methyl linoleate (C18:2, CH₃(CH₂)₄CH = CHCH₂CH = CH(CH₂)₇COOH) and methyl linolenate (C18:3, CH₃CH₂CH = CHCH₂CH = CHCH₂CH = CH(CH₂)₇COOH) with respect to HPA concentration [8–10]. The overall component ratios of all the methyl esters compositions are similar to the expected ratio. However, there are some changes in each composition depending on the different ratios of the acidity and basicity, which may provide a clue for the high catalytic activity by the bifunctional synergy effect. When the HPA concentration increases outside the ZIF-8 surface or HPA used itself, the ester compositions of the saturated fatty acids (16:0 and 18:0) decrease and the shorter chains convert to the longer chain esters. However, it was found that the FAME contents of all the catalysts consist mainly of methyl oleate (C18:1) and methyl linoleate (C18:2). Especially, the esters containing double bonds such as C18:1 easily converted to the methyl esters compared to the formation of C18:2. An interesting thing in Fig. 6(b) is that the C18:1 content increases steeply starting from the HZN-2 catalyst with a significant increase of the total FAME content, which can be due to the change to stronger acidic properties (Table 2). Generally, this is because the double bonds have an electron donating group which can facilitate the reaction rate of the transesterification, and this reaction can be improved with the presence of strong acidic sites [50]. The basicity facilitates the formation of C18:2 confirmed by the result from the base catalysts of ZIF-8 and MgO [48]. The optimized ratio where the C18:2 amount is relatively high was 1:2 = ZIF-8:HPA. Then, a sudden decrease of the C18:2 amount was found to correlate with the C18:1 amount increase by the trade-off effect with the strong acid capacity [8–10]. Therefore, we could insist that the strong acidity with sufficient basic sites can facilitate a formation of the methyl oleate (C18:1) with a certain amount of methyl linoleate (C18:2), which decides the total FAME amount and quality through synergy effect of the bifunctional HZN.

The reusability of catalysts has been a concern in the heterogeneous catalyst area. To meet this concern, we investigated the stability for the most active HZN-2. Fig. 6(c) shows the recyclability of the transesterification of rapeseed oil for 5 repeats with the total FAME content and composition. In the recycle test, we were able to easily separate the catalysts from the resultant mixture products due to the insoluble property of HZN. The collected catalyst was dried and reused for the new transesterification of rapeseed oil. Of note, we refilled new reactants to run each new reaction under the same conditions as the first test. After 5 recycling tests, there was no noticeable decrease in the catalytic activity or a change in the composition of FAME contents, indicating that the acidic and basic sites maintain the catalytic activity. Fig. S12 presents the FT-IR spectra for HZN-2 after 5 reaction cycles. The HZN-2 show similar FT-IR spectra without a significant intensity reduction even after 5 recycling tests, indicating a high stability resulting from the strong chemical bonding between ZIF-8 and HPA.

3.5. Catalytic activity on benzyl alcohol oxidation

We also employed HZN-1, 2, 3, and 4 to a benzyl alcohol oxidation reaction to demonstrate the importance of bi-functionality in other catalyst fields. In general, the oxidation of benzyl alcohol toward the desired product (i.e., benzaldehyde), a versatile chemical intermediate, is an important reaction in the industry, where chlorine-free benzyl aldehyde is widely used in the manufacture of pharmaceuticals and flavoring chemicals [19,51–53]. For the benzyl alcohol oxidation, hydrogen peroxide (H₂O₂) was used as an environmentally-friendly oxidant with a benzyl alcohol to H₂O₂ ratio of 4.6: 6.0 with the addition of 4.6 mmol of each catalyst. The reaction conditions were fixed to 75 °C

and 2 h. Fig. 6(d) shows the benzyl alcohol conversions and benzyl aldehyde yields on the left y-axis along with corresponding surface area values on the right y-axis for pure HPA, ZIF-8, and HZN-1, 2, 3, and 4. The HZN-1, 2, 3, and 4 show a liquid–solid phase throughout the reaction, performing over 95% conversion and a higher selectivity of benzaldehyde compared to those of the pure HPA and ZIF-8. This excellent catalytic activity might have resulted from the bi-functionality which elevates the oxidative cleavage of benzyl alcohol to benzaldehyde in the presence of H₂O₂ oxidant. At the HPA shell, W and P ions are converted to a peroxy complex which favorably reacts with the benzyl alcohol to produce a benzaldehyde intermediate by losing H₂O molecule [54–56]. Simultaneously, the activated N species in the ZIF-8 core that is from the interaction with HPA can be transformed to an N–O₂ adduct transition state by the adsorption and activation of a molecular oxygen [57]. Finally, the chemically reactive N–O₂ state attacks the H atom at alcohol to produce benzaldehyde and water [58]. In particular, upon this synergistic mechanism, the HZN-2 catalyst exhibits the best performance with a high selectivity for benzaldehyde of 90.2%, which is a similar trend to the FAME production, depending on the acidity/basicity composition and surface area. These results suggest that well-designed, bifunctional HZN with both acid/base functionalities and a large surface area can also lead to great catalytic activity in oxidation reaction systems.

4. Conclusion

We designed a new core-shell structured heterogeneous catalyst using a simple HPA functionalization method on ZIF-8 nanoparticles. The HPA functionalization makes the ZIF-8 nanoparticles increase in bifunctional catalytic activity, but decreases the surface area, therefore the proper HPA concentration in the heterogeneous catalyst would have the best catalytic activity in the transesterification process by rapeseed oil for an efficient biodiesel production. The X-ray studies (i.e., XANES and XPS) revealed that strong O–N bonding between the Keggin structure in the HPA and imidazole group in the ZIF-8 nanoparticles allows the formation of HZN. With the strong interaction, the HZN became insoluble in hydrophilic solvents, such as alcohols and water, which originally dissolve pure HPA powders, overcoming the limitation of pure HPA in catalytic applications. The HZN with sufficient bi-functionality and surface area show a high FAME conversion with high recyclability. This simple catalytic functionalization strategy can be applicable to other MOF particles, which allows the production of various catalysts showing high performance and stability.

Acknowledgments

This work was supported by the New and Renewable Energy R&D Program (Grant 20113020030020) under the Ministry of Knowledge Economy and the National Research Foundation (NRF) of South Korea grant funded by the Ministry of Science, ICT and Future Planning (NRF-2017R1A4A1014569, NRF-2017R1D1A1B06028030, NRF-2018M3A7B4071535).

Appendix A. Supplementary data

Supplementary material related to this article can be found, in the online version, at doi:<https://doi.org/10.1016/j.apcatb.2018.09.071>.

References

- [1] E.L. Margelefsky, R.K. Zeidan, M.E. Davis, Chem. Soc. Rev. 37 (2008) 1118–1126.
- [2] A. Crake, K.C. Christoforidis, A. Kafizas, S. Zaferatos, C. Petit, Appl. Catal. B 210 (2017) 131–140.
- [3] M. Robinson, J.E. Hensley, J.W. Medlin, ACS Catal. 6 (2016) 5026–5043.
- [4] R.A. Sheldon, Chem. Soc. Rev. 41 (2012) 1437–1451.
- [5] N. Boz, N. Degirmenbası, D.M. Kalyon, Appl. Catal. B 138–139 (2013) 236–242.
- [6] D. Wang, B. Wang, Y. Ding, H. Wu, P. Wu, Chem. Comm. 52 (2016) 12817–12820.

[7] L. Xu, W. Li, J. Hu, K. Li, X. Yang, F. Ma, Y. Guo, X. Yu, Y. Guo, *J. Mater. Chem.* 19 (2009) 8571–8579.

[8] J. Gardy, A. Hassanpour, X. Lai, M.H. Ahmed, M. Rehan, *Appl. Catal. B* 207 (2017) 297–310.

[9] Q. Zhao, H. Wang, H. Zheng, Z. Sun, W. Shi, S. Wang, X. Wang, Z. Jiang, *Catal. Sci. Technol.* 3 (2013) 2204–2209.

[10] F. Su, S. An, D. Song, X. Zhang, B. Lu, Y. Guo, *J. Mater. Chem. A Mater. Energy Sustain.* 2 (2014) 14127–14138.

[11] Y. Liu, S. Liu, D. He, N. Li, Y. Ji, Z. Zheng, F. Luo, S. Liu, Z. Shi, C. Hu, *J. Am. Chem. Soc.* 137 (2015) 12697–12703.

[12] A.F. Lee, J.A. Bennett, J.C. Manayil, K. Wilson, *Chem. Soc. Rev.* 43 (2014) 7887–7916.

[13] A.W. Go, S. Sutanto, L.K. Ong, P.L. Tran-Nguyen, S. Ismadji, Y.-H. Ju, *Renew. Sustain. Energy Rev.* 60 (2016) 284–305.

[14] E.G. Al-Sakkari, S.T. El-Sheltawy, N.K. Attiab, S.R. Mostaf, *Appl. Catal. B* 206 (2017) 146–157.

[15] M. Huang, J. Luo, Z. Fang, H. Li, *Appl. Catal. B* 190 (2016) 103–114.

[16] T. Okuhara, *Chem. Rev.* 102 (2002) 3641–3666.

[17] J. Li, X. Wang, W. Zhu, F. Cao, *ChemSusChem* 2 (2009) 177–183.

[18] A. Alsalme, E.F. Kozhevnikova, I.V. Kozhevnikov, *Appl. Catal. A Gen.* 349 (2008) 170–176.

[19] Patel, S. Singh, *Ind. Eng. Chem. Res.* 52 (2013) 10896–10904.

[20] L. Xu, W. Li, J. Hu, X. Yang, Y. Guo, *Appl. Catal. B* 90 (2009) 587–594.

[21] G. Corroa, U. Pal, N. Tellez, *Appl. Catal. B* 129 (2013) 39–47.

[22] N.R. Shiju, A.H. Alberts, S. Khalid, D.R. Brown, G. Rothenberg, *Angew. Chem.* 123 (2011) 9789–9793.

[23] A. Micek-Ilnicka, B. Gil, *Dalton Trans.* 41 (2012) 12624–12629.

[24] U. Sen, M. Erkarta, C.-W. Kung, V. Ramani, J.T. Hupp, O.K. Farha, *ACS Appl. Mater. Interfaces* 8 (2016) 23015–23021.

[25] Q. Deng, G. Nie, L. Pan, J. Zou, X. Zhang, L. Wang, *Green Chem.* 17 (2015) 4473–4481.

[26] W.S. Chi, S.J. Kim, S.J. Lee, Y.S. Bae, J.H. Kim, *ChemSusChem* 8 (2015) 650–658.

[27] A.E.R.S. Khder, H.M.A. Hassan, M.S. El-Shall, *Appl. Catal. A Gen.* 411–412 (2012) 77–86.

[28] A. Bielanski, Lubanska, J. *Mol. Catal. A Chem.* 224 (2004) 179–187.

[29] S.R. Matković, L.E. Briand, M.Á. Baháres, *Mater. Res. Bull.* 46 (2011) 1946–1948.

[30] P. Kiisgens, M. Rose, I. Senkovska, H. Fröde, A. Henschel, S. Siegle, S. Kaskel, *Microporous Mesoporous Mater.* 120 (2009) 325–330.

[31] Y.S. Bae, A.Ö. Yazaydin, R.Q. Snurr, *Langmuir* 26 (2010) 5475–5483.

[32] F. Zhang, Y. Jin, J. Shi, Y. Zhong, W. Zhu, M.S. El-Shall, *Chem. Eng. J.* 269 (2015) 236–244.

[33] X.-L. Yang, L.-M. Qiao, W.-L. Dai, *Microporous Mesoporous Mater.* 211 (2015) 73–81.

[34] H. Wan, C. Chen, Z. Wu, Y. Que, Y. Feng, W. Wang, L. Wang, G. Guan, X. Liu, *ChemCatChem* 7 (2015) 441–449.

[35] T. Ilkenhans, B. Herzog, T. Braun, R. Schlogl, *J. Catal.* 153 (1995) 275–292.

[36] U. Mioc, M. Davidovic, N. Tjapkin, Ph. Colomban, A. Novak, *Solid State Ion.* 46 (1991) 103–109.

[37] M. Vasilopoulou, A. Soultati, D.G. Georgiadou, T. Stergiopoulos, L.C. Palilis, S. Kennou, N.A. Stathopoulos, D. Davazoglou, P. Argitis, *J. Mater. Chem. A* 2 (2014) 1738–1749.

[38] H. Huang, Y.-C. Lu, A.-J. Wang, J.-H. Liu, J.-R. Chen, J.-J. Feng, *RSC Adv.* 4 (2014) 11872–11875.

[39] Q. Wang, P. Zhang, Q. Zhuo, X. Lv, J. Wang, X. Sun, *Nano-micro Lett.* 7 (2015) 368–373.

[40] S. Luanwuthi, A. Krittayavathananon, P. Srimuk, M. Sawangphruk, *RSC Adv.* 5 (2015) 46617–46623.

[41] H. Yabuta, M. Uesugi, H. Naraoka, M. Ito, A.L.D. Kilcoyne, S.A. Sandford, F. Kitajima, H. Mita, Y. Takano, T. Yada, Y. Karouji, Y. Ishibashi, T. Okada, M. Abe, *Earth Planets Space* 66 (2014) 156.

[42] S.-Y. Chen, R.-J. Chen, W. Lee, C.-L. Dong, A. Gloter, *Phys. Chem. Chem. Phys.* 16 (2014) 3274–3281.

[43] P.A. Jalil, N. Tabet, M. Faiz, N.M. Hamdan, Z. Hussain, *Appl. Catal. A Gen.* 257 (2004) 1–6.

[44] K. Zhou, B. Mousavi, Z. Luo, S. Phatanasri, S. Chaemchuen, F. Verpoort, *J. Mater. Chem. A* 5 (2017) 952–957.

[45] J.I. Di Cosimo, V.K. Di'ez, C. Ferretti, C.R. Apesteguia, *Catalysis* 26 (2014) 1–28.

[46] K. Fan, J. Liu, X. Yang, L. Rong, *RSC Adv.* 5 (2015) 37916–37924.

[47] D.M. Alonso, M.L. Granados, R. Mariscal, A. Douhal, *J. Catal.* 262 (2009) 18–26.

[48] M. Verziu, B. Cojocaru, J. Hu, R. Richards, C. Ciulescu, P. Filip, V.I. Parvulescu, *Green Chem.* 10 (2008) 373–381.

[49] H. Jeon, D.J. Kim, S.J. Kim, J.H. Kim, *Fuel Process. Technol.* 116 (2013) 325–331.

[50] K. Xu, Y. Fang, Z.C. Yan, Z.G. Zha, Z.Y. Wang, *Org. Lett.* 15 (2013) 2148–2151.

[51] G. Chen, S. Wu, H. Liu, H. Jiang, Y. Li, *Green Chem.* 15 (2013) 230–235.

[52] A. Dhakshinamoorthy, M. Alvaro, H. Garcia, *ACS Catal.* 1 (2011) 48–53.

[53] Y. Leng, P. Zhao, M. Zhang, J. Wang, *J. Mol. Catal. A Chem.* 358 (2012) 67–72.

[54] Manisha P. Chaudhari, Sudhirprakash B. Sawant, *Chem. Eng. J.* 106 (2005) 111–118.

[55] R. Zbigniew, *J. Am. Chem. Soc.* 82 (1960) 1267–1277.

[56] C. Venturello, M. Ricci, J. Org. Chem. 51 (1986) 1599–1602.

[57] M. Li, F. Xu, H. Li, Y. Wang, *Catal. Sci. Technol.* 6 (2016) 3670–3693.

[58] J. Long, X. Xie, J. Xu, Q. Gu, L. Chen, X. Wang, *ACS Catal.* 2 (2012) 622–631.